# Analysis Of Time-Resolved Data For Tomographical Image Reconstruction Of Opaque Phantoms And Finite Absorbers In Diffusive Media

B. B. Das, J. Dolne, R. L. Barbour*, H. L. Graber*, J. Chang*, M. Zevallos, F. Liu and R. R. Alfano

The Institute for Ultrafast Spectroscopy and Lasers, New York State Center for Advanced Technology for Ultrafast Photonic Materials and Applications, City College of New York, 138 St. and Convent Ave., New York, NY 10031.

*Department of Pathology, SUNY Health Science Center at Brooklyn, Brooklyn, NY 11203

## Abstract

Experimental time-resolved data was used for direct reconstruction of images of laboratory phantoms in highly scattering media. Using different time zones of the temporal profiles, computed images were calculated by solving a one-step linear perturbation equation derived from transport theory. In nearly all cases tested, high quality reconstructions were obtained even for highly underdetermined problems.

**Keywords**: Time-resolved tomography, streak camera, highly scattering media, tomographical image reconstruction

## 1. Introduction

Over the past several years there is a surge of activities in two directions - using early (snake) light [1] and diffuse light - to obtain images in highly scattering media. One way is to directly view the object using early (snake) light by time [1, 2] and space gating [2]. Early light imaging have also been accomplished using streak camera [3-5], stimulated Raman effect [6], and holographic gate [7]. In the other direction, diffuse light imaging is accomplished by several approaches, such as cw light [8], modulated photon density wave imaging [9-10], and forward and inverse image reconstructions [11-18].

In this paper we present, for the first time, tomographic reconstructions of opaque and partially absorbing phantoms in highly scattering media using time-resolved data in various numerical algorithms. The numerical algorithms used here are: projection onto convex sets (POCS), simultaneous algebraic reconstruction technique (SART), and conjugate gradient descent (CGD), and a linear perturbation model [11, 13, 14]. A SART-type algorithm developed over the past few years [15] using the relative changes instead of the absolute changes in the scattered signals in order to minimize the effect of imperfect detector calibrations and source fluctuations is also used in this work.

In a linear perturbation model, the detected signal can be expanded in a Taylor series about an optical property $x$ as follows:

$$y = y^0 + \sum_i^N \frac{\partial y^0}{\partial x_i}(x_i - x_i^0) + \frac{1}{2}\sum_i^N \sum_j^N \frac{\partial^2 y^0}{\partial x_i \partial x_j}(x_i - x_i^0)(x_j - x_j^0) + \ldots \quad (1)$$

where $y$ is the signal with the phantom in the medium, $y^0$ is the reference signal without the phantom, and $x$ is the optical property that is varied. The sum is over all the voxels in the medium. If we ignore the voxel-voxel interaction, we can drop the higher order terms, and this yields a first order linear perturbation equation:

$$y^0 - y = -\sum_i^N \frac{\partial y^0}{\partial x_i}(x_i - x_i^0) \quad (2)$$

In matrix formulation it can be written as:

$$\Delta y = \boldsymbol{w}^T \Delta \boldsymbol{x}, \quad (3)$$

where $\boldsymbol{w}^T$ is called the weight function. The weight functions for each voxel, as shown below, were obtained using transport theory where Monte Carlo simulations were used to obtain the collision densities.



0-8194-1736-X/95/$6.00

The weight functions are defined as:

$$w_{ij}^{cw} = \frac{S_{0j} F_{0i} F_{ij}}{4\pi \Sigma_{ti}^2 V_i}, \quad \text{CW case} \tag{4}$$

$$\text{and} \quad w_{ij}(t) = \frac{S_{0j}}{4\pi \Sigma_{ti}^2 V_i} \int_0^t F_{0i}(\tau) F_{ij}(t-\tau) d\tau, \quad \text{Time domain case} \tag{5}$$

where $F_{oi}$ is the number of collisions in $V_i$ due to a single photon launched from the source,

$F_{ij}$ is the number of collisions in $V_i$ due to a single photon launched from the detector,

$S_{oj}$ is the source strength (photons/second),

and $\Sigma_{ti}$ is the macroscopic total cross section in $V_i$.

The expressions for the four reconstruction algorithms are given as follows:

1. *Projection onto convex sets (POCS).*

POCS [13] is a sequential projection method which reaches the intersection point of $L$ constraint sets by projecting the current estimate of the solution onto each set $C_l$ (a set which satisfies the $l^{\text{th}}$ constraint), $l = 1, 2, \ldots, L$, sequentially and iteratively. By letting $\Delta x^n$ represent the estimate at the $n^{\text{th}}$ iteration, each step in POCS can be represented by:

$$\Delta \boldsymbol{x}^{n+1} = P_L P_{L-1} \ldots P_1 \boldsymbol{x}^n \tag{6}$$

Here, $P_l$ represents the projection operator onto $C_l$, such that $P_l \Delta \boldsymbol{x}^n$ is the element in $C_l$ that is closest to $\Delta \boldsymbol{x}^n$.

2. *Simultaneous algebraic reconstruction technique (SART).*

The SART algorithm [11] is a simultaneous projection method that introduces two normalization factors into the backprojection step that account for the particular source-detector geometry for each projection. The update is computed according to the following equation:

$$\Delta x_j^{n+1} = \Delta x_j^n + \frac{\sum_i w_{ij} \dfrac{\Delta y_i - \sum_j w_{ij} \Delta x_j^n}{\sum_j w_{ij}}}{\sum_i w_{ij}} \tag{7}$$

3. *Conjugate gradient descent (CGD).*

The CGD update is computed according to the conjugate gradient direction **d**,

$$\mathbf{d}^n = -\mathbf{g}^{n-1} + \beta^n \mathbf{d}^{n-1}, \text{ where } \beta^n = \frac{\left\|\mathbf{g}^n\right\|^2}{\left\|\mathbf{g}^{n-1}\right\|^2}, \quad \mathbf{g}^n = \frac{\partial E}{\partial \Delta \mathbf{x}} = \mathbf{W}^{\mathrm{T}} (\Delta \mathbf{y}^n - \Delta \mathbf{y}),$$

$$\Delta \mathbf{y}^n = \mathbf{W} \Delta \mathbf{x}^n, \quad \Delta \mathbf{x}^n = \Delta \mathbf{x}^{n-1} - \alpha^n \mathbf{d}^n, \quad \alpha^n = \frac{\left(\mathbf{g}^n\right)^{\mathrm{T}} \mathbf{d}^n}{\left\|\mathbf{W}\, \mathbf{d}^n\right\|^2}. \tag{8}$$

where $\mathbf{g}^n$ is the gradient vector, and $\alpha$ is called the step-size, which must be chosen appropriately to guarantee convergence. Theoretically, this algorithm should converge after a number of iterations less than or equal to the number of unknowns.

4. *SART-type.*

The SART-type algorithm considers the relative change in a detector response. It was developed in recognition that, experimentally, it may be difficult in all cases to accurately determine absolute differences in detector readings [15]. The solution obtained is unitless, unlike those obtained based on an absolute detector differences whose units are inverse length. We recognize that this could make efforts to update a solution difficult, but we consider this a useful tradeoff considering the alternative, which in some cases might be no answer at all. The update is computed according to the following expression:

$$\Delta s_j^{n+1} = \Delta s_j^n + \frac{\sum_i w_{ij} \left[ \frac{\Delta y_i}{y_i^0} - \frac{\sum_j w_{ij} \cdot \Delta s_j^n}{\sum_j w_{ij}} \right]}{\sum_i w_{ij}} \tag{9}$$

## 2. Experimental Methods

The experimental set-up for our tomographic measurements is displayed in Figure 1. Time-resolved light

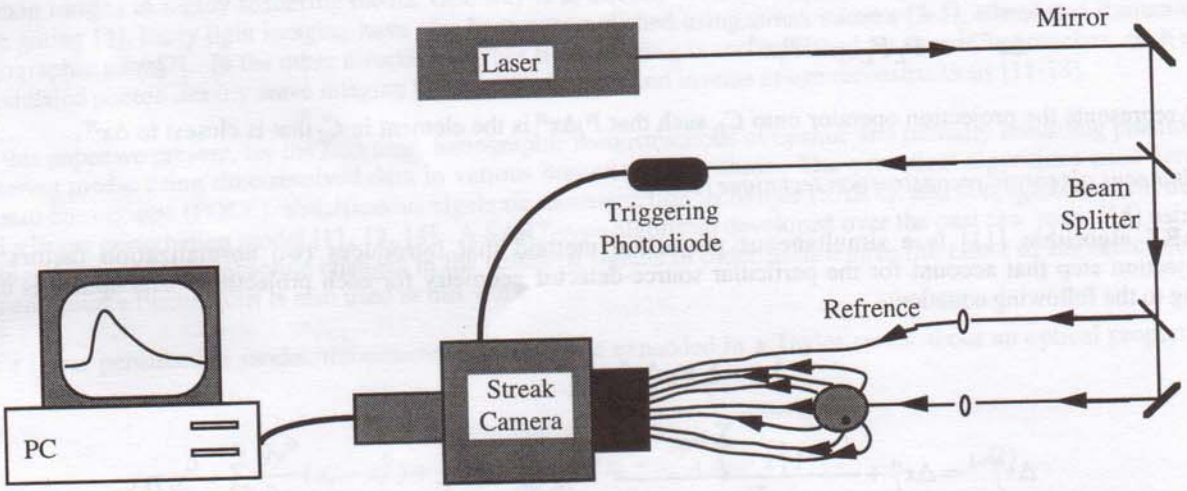


Figure 1. Experimental setup for tomographic measurements with a colliding pulse mode locked (CPM) dye laser and streak camera.

scattering measurements were performed at 625 nm using a femtosecond CPM laser and a synchroscan streak camera coupled to a cooled CCD camera. A part of the incident beam was used to trigger the streak camera and another part was used as a reference beam. Two cylindrical cells-a 75 mm diameter plastic cell (painted black) and a 89 mm diameter aluminum cell (anodized black)- were filled with intralipid solution to a final concentration of 0.15% solids. The transport mean free path ($l_t = 1/\Sigma_s(1\text{-}g)$) under these conditions is 4.5 mm. The dimensions of the two sample cells are shown in Figure 2. Two aluminum rods of 4.5 mm and 2 mm diameter were painted black to form two opaque phantoms. Glass tubes with 5 mm outer diameter and 3 mm inner diameter were filled with a mixture of 0.15% intralipid and two different concentrations (1 and 0.5 ml) of a blue dye DQOCI (Exciton) to form two partially absorbing phantoms. The absorption lengths ($l_a$) of these two phantoms were 2.3 and 4.6 mm, respectively. A 200 micron optical fiber was used to deliver ~ 100 fs laser pulses at 82 MHz repetition rate to the scattering medium. Seven detector fibers (600 micron diameter) were arranged in a plane perpendicular to the cylindrical axis at angles $\theta_i = i\pi/4$, where i = 1, 2, ..., 7, surrounding the scattering object from the source direction (Fig. 2).

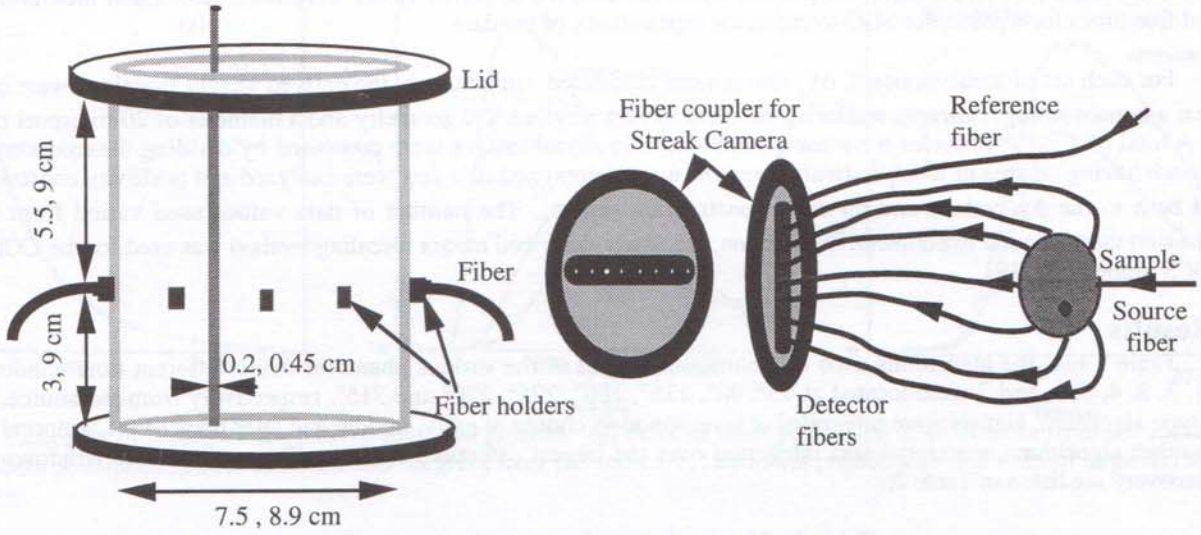


Figure 2. A schematic of the sample cell and the optical fiber connection from the source to the steak camera. Smaller numbers listed with the sample cell refer to the dimensions of the smaller cell used.

Four different experiments were performed using the two cells with various opaque and partially absorbing phantoms. A schematic diagram of various phantom locations is given in Figure 3. In the first experiment, the 4.5 mm opaque rod was placed at the center of the scattering medium (75 mm cell).

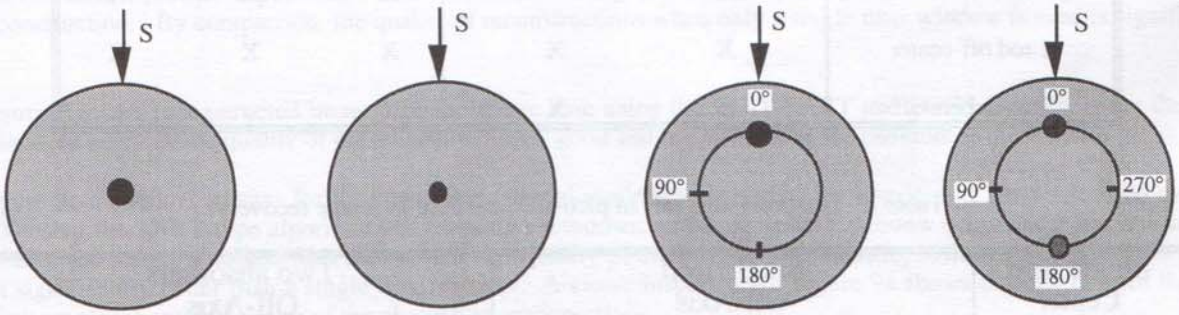


Figure 3. A schematic display of the four different phantoms: (a) 4.5 and (b) 2 mm diameter aluminum rods painted black and located at the center; (c) 4.5 mm rod at an off axis position; (d) two-rod phantom.

A cooled CCD camera coupled to a computer was used to record the temporal profiles $y_i(t)$ of the scattered light entering the seven detector fibers simultaneously arranged in a linear fashion in front of the streak camera slit. A part of the beam was used as a reference to calculate the zero time and to keep track of power fluctuations. The temporal profiles $y_i^o(t)$ for the reference medium were recorded without the opaque rod inside the scattering medium. Similar measurements were performed with the small black rod at the center of the small cell. The third experiment was performed by measuring various temporal profiles with the large opaque rod at a radial distance of 25 mm between the center and the source. This measurement was repeated after positioning the rod at 90° and 180° on a 25 mm circle in order to accomplish 3 different source-detector configurations (SDC). The fourth experiment was done with the two partial absorbers placed at two diametrically opposite locations 25 mm from the center as shown in Fig. 3. The measurements were repeated after positioning the pair of absorbers at 90°, 180° and 270° to accomplish 4 different SDC. The reference measurements were obtained in this case by placing the same glass tubes filled with 0.15% intralipid in place of the partial absorbers.

Because of large differences in the signals from various detector fibers, each measurement was performed in two steps. Signals from the 45° and 315° fibers were integrated for 30 seconds and that from the other fibers were integrated for about 120

seconds to improve the signal to noise ratio. In order to avoid the influence of the strong signals from the 45° and 315° fibers on the others, these two fibers were not present when the data for the other fibers were recorded. Each measurement was repeated five times for a particular SDC to check the repeatability of the data.

For each set of measurements, $\Delta y_i$ values were calculated. In all cases, the derived weight functions were computed based on a nonabsorbing, isotropic scattering medium having a cylindrical geometry and a diameter of 20 transport mean free paths. A total of 2 x $10^8$ histories were computed. Cross-sectional images were computed by dividing the cylinder into 400 voxels each having an area of $\pi/4(l_t)^2$. In all cases, the underdetermined data sets were analyzed and positivity constraints were applied both to the $\Delta y_i$ values and on the reconstruction results. The number of data values used varied from 56 to 84 depending on the particular experiment. In addition, the newly described matrix rescaling method was used for the CGD, SART and POCS algorithms [19].

## 3. Results

Table 1 lists the algorithms used to reconstruct images of the various phantoms using different time windows. The fibers 1, 3, 2, 4, 5, 6, and 7 were located at 45°, 90°, 135°, 180°, 225°, 270° and 315°, respectively from the source. For the SART-type algorithm, signals were integrated at time windows chosen at early, middle and later parts of the temporal profiles. For the other algorithms, the signal was integrated over the largest detection window. The various time windows used for image recovery are listed in Table 2.

Table 1. Matrix of algorithms and phantom studies.

| Experiment | SART Type ($\Delta y/y^0$) No. of Windows 1 | 3 | CGD | SART ($\Delta y$) Largest time window | POCS |
|---|---|---|---|---|---|
| Large rod center | X | | X | X | X |
| Small rod center | X | | X | X | X |
| 1 rod off-center | X | X | X | X | X |
| 2 absorbers off | X | X | X | | |

Table 2. Temporal intervals in pico-seconds used in image recovery.

| Single Rod Center | | Single Rod Off-Axis | | | | Two absorbers Off-Axis | | | |
|---|---|---|---|---|---|---|---|---|---|
| Fiber | Middle | Fiber | Early | Middle | Late | Fiber | Early | Middle | Late |
| 1, 7 | 600-700 | 1, 7 | 200-270 | 700-770 | 1530-1600 | 1, 7 | 300-400 | 700-800 | 1300-1400 |
| 3, 6 | 600-700 | 3, 6 | 300-370 | 800-870 | 1530-1600 | 3, 6 | 400-500 | 800-900 | 1500-1600 |
| 2, 5 | 600-700 | 2, 5 | 450-520 | 800-870 | 1530-1600 | 2, 5 | 600-700 | 1400-1500 | 2000-2100 |
| 4 | 600-700 | 4 | 500-570 | 800-870 | 1530-1600 | 4 | 700-800 | 1400-1500 | 2200-2300 |

A typical set of temporal profiles for various fibers is displayed in Figure 4a-c. The computed coefficients of variation for replicate measurements were less than 5%. Figure 4c displays two temporal profiles from the 180° fiber for the reference medium and for the case with the phantom inside. In the presence of the phantom, a significant reduction in the signal intensity occurs.

Figure 5(a)-(b) displays the reconstructed images of the large rod (4.5 mm) and small rod (2 mm) using the SART-type algorithm. Reconstructed images were obtained using the time window listed in Table 2. In both cases the position of the phantom is correctly identified. The diameter of the central disk (brightest) matches that of the large rod. For the small rod, the voxel size is larger than the rod diameter. The quality of the reconstructed image in this case was significantly poorer than for the large rod.

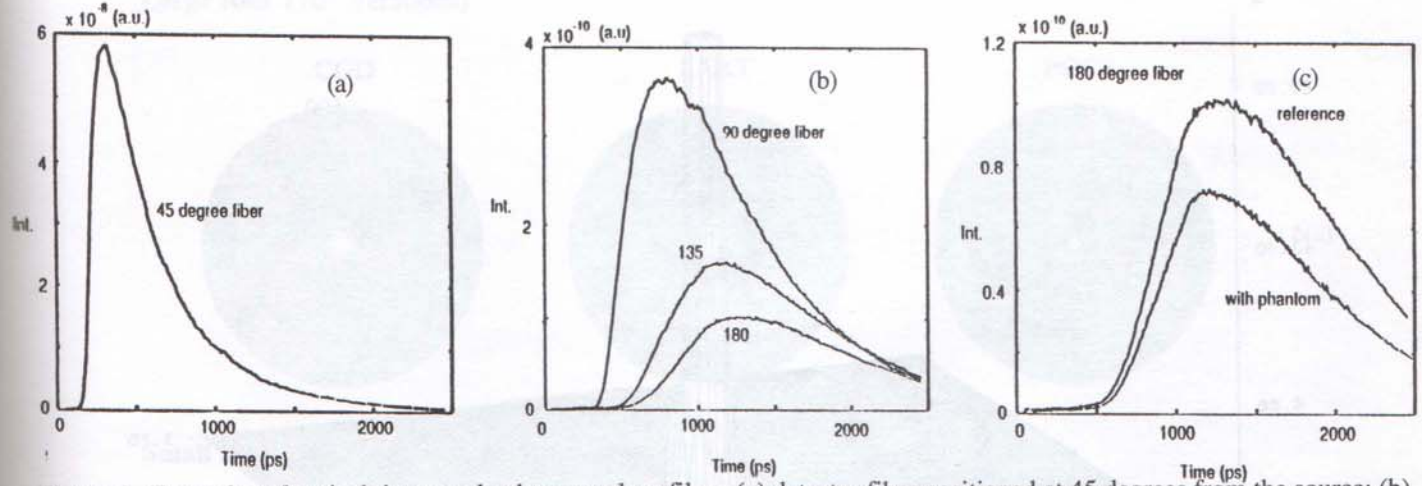


Figure 4. Examples of typical time-resolved temporal profiles: (a) detector fiber positioned at 45 degrees from the source; (b) detector fibers positioned at 90°, 135° and 180° degrees from the source; (c) temporal profile with and without large rod located in the center.

Figures 6a,b show the reconstructed images of the large and small rod phantoms using the CGD, POCS and SART algorithms for the largest time window (time-integrated). The quality of the images in all cases was good, though reconstructions using the POCS algorithm produced the least edge artifact. A comparison of the ratio of the computed cross sections (large/small rod) showed a good correlation with the ratio of the diameter of the rods. The latter value of 2.25 compares to ratios of 2.7 (CGD), 2.4 (SART) and 3.0 (POCS).

Figure 7a-c display reconstructions of the large rod using the SART type algorithm when located in an off-axis position. Results in Figure 7a were obtained using three different time windows while Figures 7b and 7c were obtained using an early and late time window, respectively. The results seen in Figure 7a are surprisingly noise free and represents a highly accurate reconstruction. By comparison, the quality of reconstructions when only a single time window is used is significantly poorer.

Figure 8 shows reconstructed images for the above case using the CGD, SART and POCS algorithms for the time-integrated data. In all cases the quality of the reconstruction is good and the position of the phantom is quite accurate.

Figure 9a-c displays images for the case of two partial absorbers located on the line joining the source and the 180° fiber (Fig. 3) using the SART-type algorithm and three time windows, and a single time window using early and late arriving light. Similar to the results obtained with the off-axis, the quality of the image obtained using multiple time windows is very good and is significantly better than a single time window. A closer inspection of Figure 9a shows that the ratio of the peak heights correlates closely with the ratio of the absorption cross sections.

Figure 10 shows the reconstructed images obtained using the time-integrated signal and the CGD algorithm. It is evident that the quality of the reconstruction obtained is significantly poorer when compared to the case with multiple time windows.

## 4. Discussion

We have investigated the quality of reconstructed images of various simply structured phantoms in highly scattering media using the time-resolved data from tomographic measurements in various numerical algorithms. Results obtained have shown that, in many cases, high quality reconstructions are achievable even for highly underdetermined data sets. These findings support and extend previous reports from our group [11, 13-15, 20] demonstrating that, using a one-step linear perturbation model derived from transport theory, sufficient information exists at the boundary of dense scattering media to permit accurate recovery of internal structure, at least for simply structured media.

Use of perturbation methods requires specification of some type of reference medium. For our experiments, reference detector intensities were directly measured simply by removing the target phantom from the medium. While this permitted an accurate specification of the $\Delta y_i$ values, determination of the correct weighting functions is more difficult. Here, these were computed using Monte Carlo methods. In the cases examined, the weight functions were computed assuming a cell diameter of 20 transport mean free pathlengths. As mentioned in the Methods, two different experimental vessels were used.

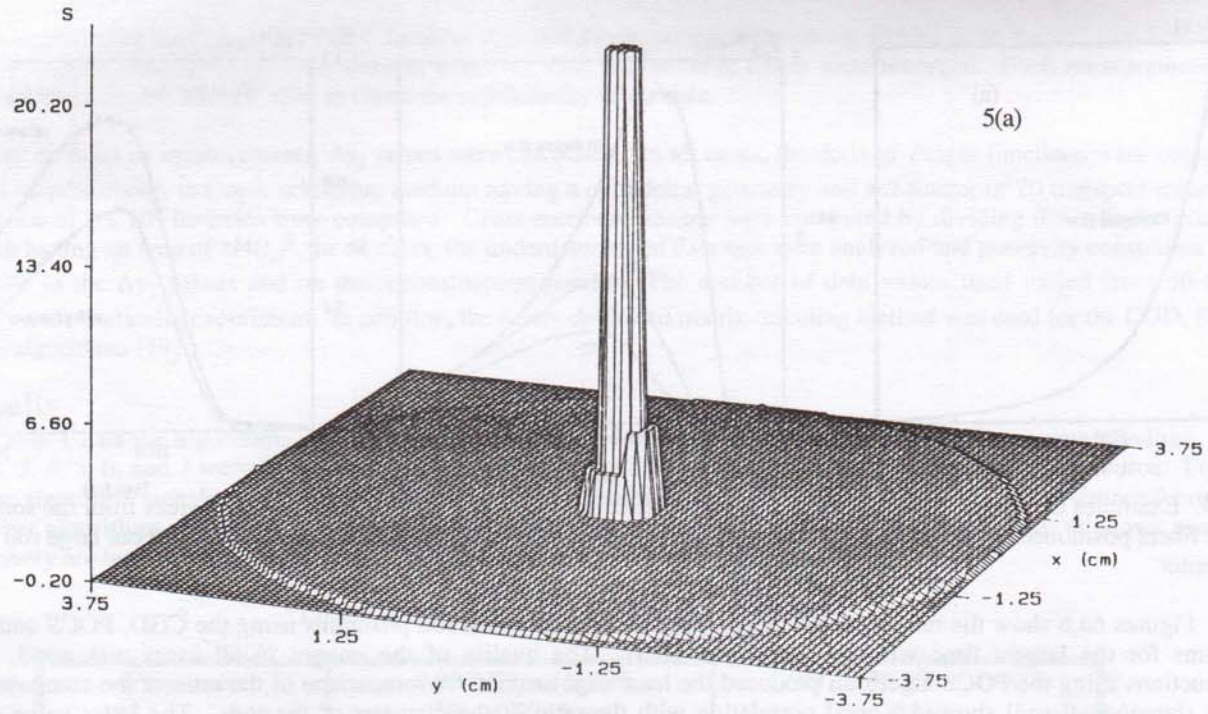


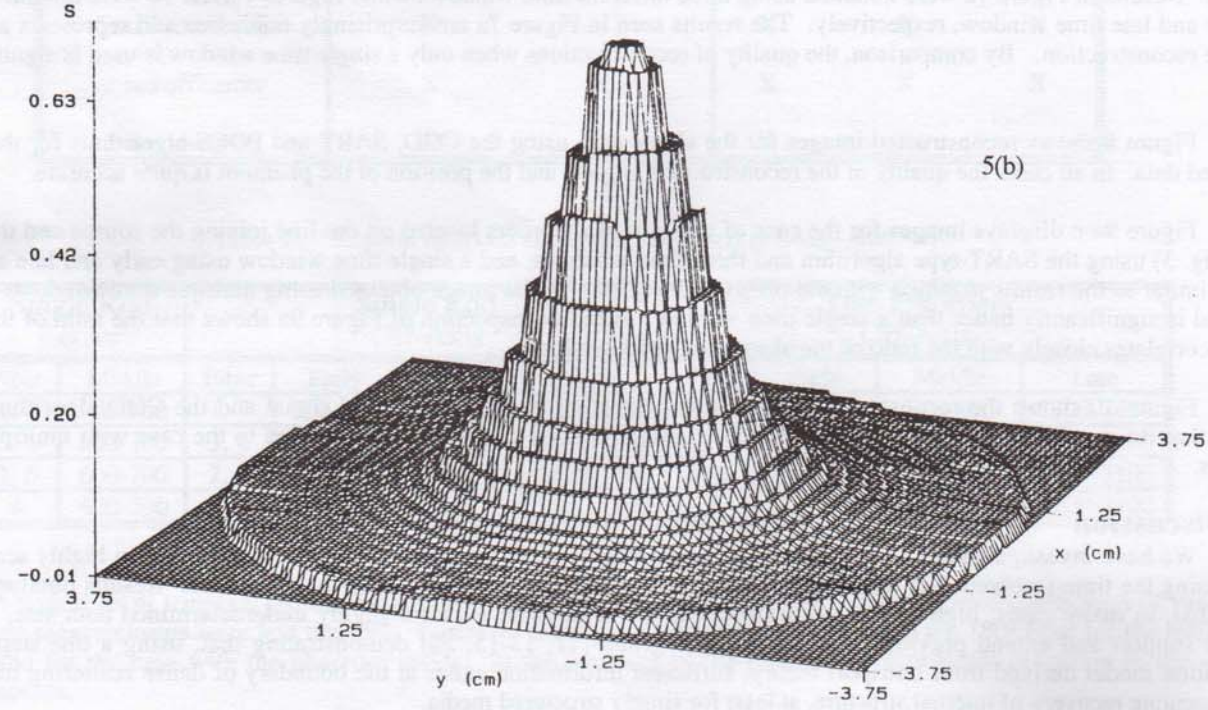


Figure 5. 3-D display of computed cross sectional images of (a) the large (4.5 mm) rod, and (b) small (2 mm) rod located at the center using time-resolved data and the SART-type algorithm.

**Large Rod** ($10^5$ Iterations)


6(a)

**Small Rod** ($10^5$ Iterations)


6(b)

Figure 6. Gray scale display of computed cross-sectional images of (a) large rod and (b) small rod obtained using time-integrated data and the CGD, SART and POCS algorithms.

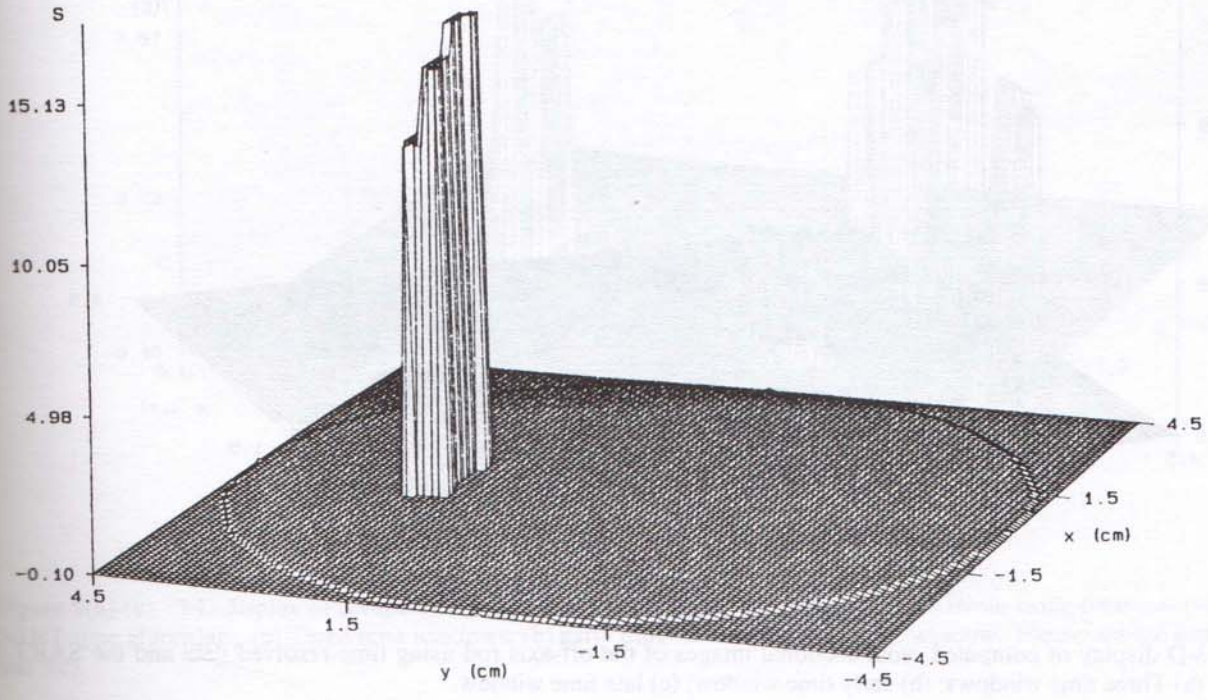


7(a)

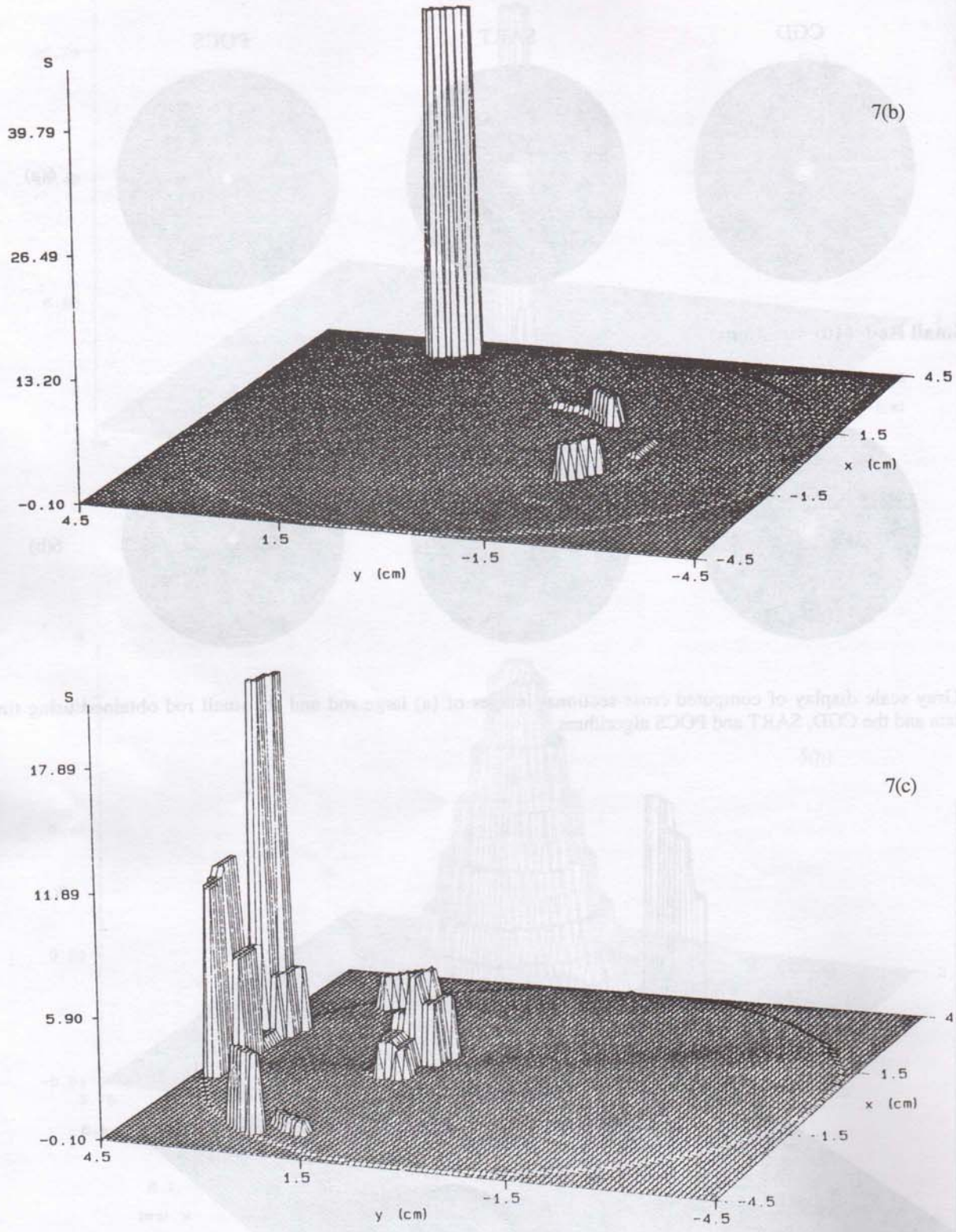


Figure 7. 3-D display of computed cross sectional images of the off-axis rod using time-resolved data and the SART-type algorithm. (a) Three time windows; (b) early time window; (c) late time window.

**Off-axis Rod** ($10^5$ Iterations)


Figure 8. Gray scale display of computed cross-sectional images of the off-axis rod using the integrated data for the largest detected time window, and the CGD, SART and POCS algorithms.

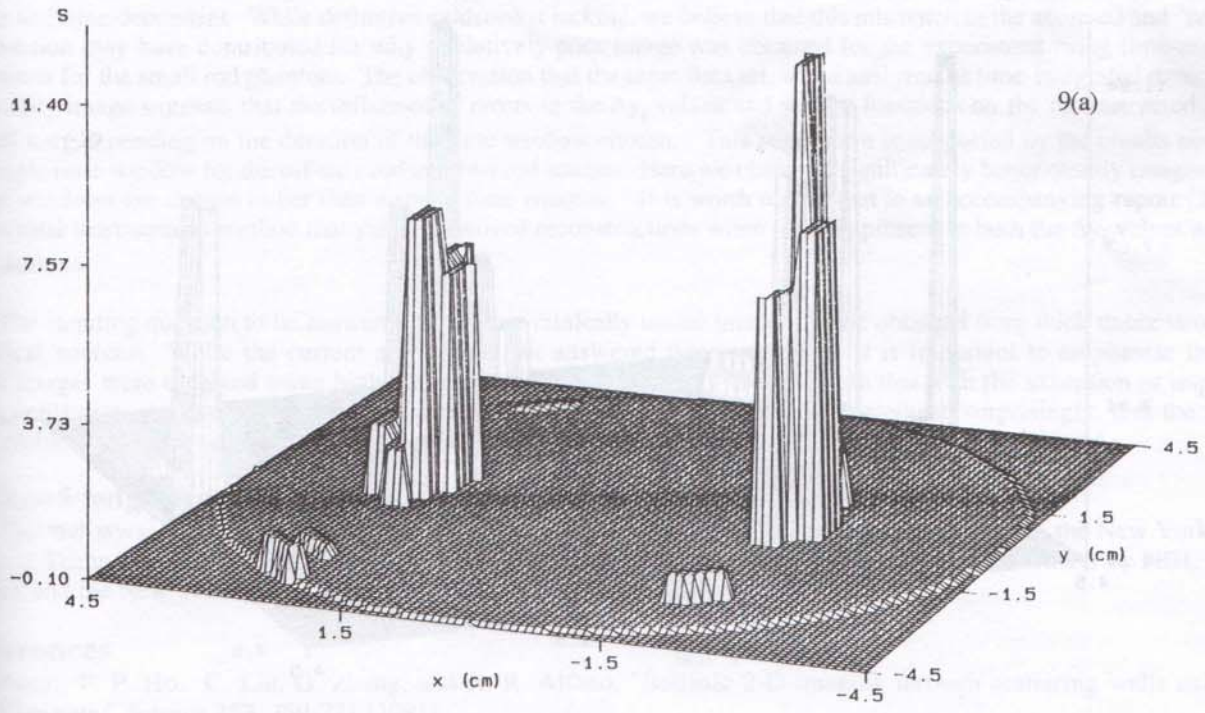


Figure 9(a)-(c). 3-D display of computed cross-sectional images of the two-absorber phantom using time-resolved data and the SART-type algorithm. (a) Three time windows; (b) early time window; (c) late time window. Please see the next page for 9(b) and 9(c)

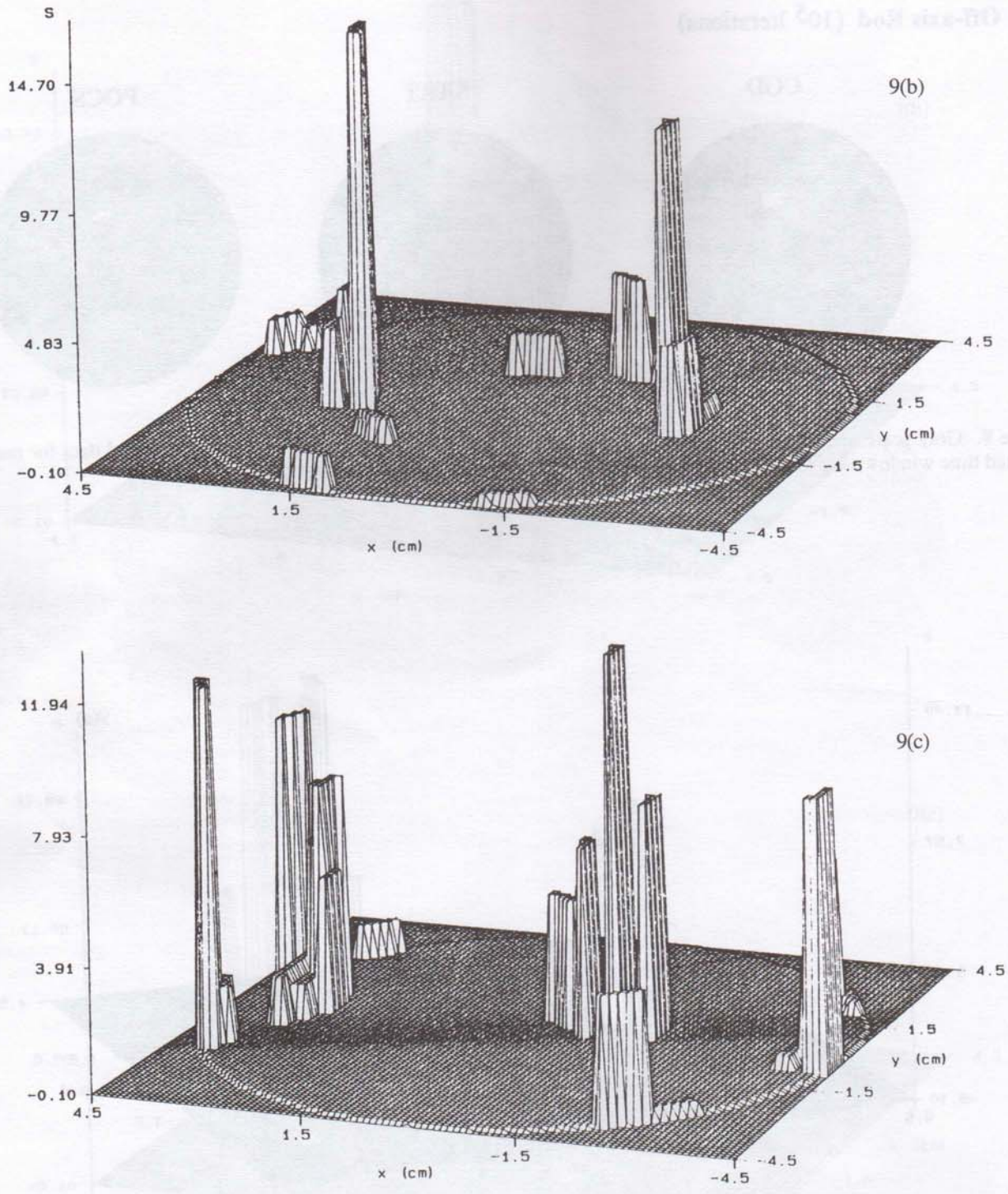


Figure 9(a)-(c). 3-D display of computed cross-sectional image of the two-absorber phantom using time-resolved data and the SART-type algorithm. (a) Three time windows; (b) early time window; (c) late time window.

**CGD: Two Absorbing Rods**

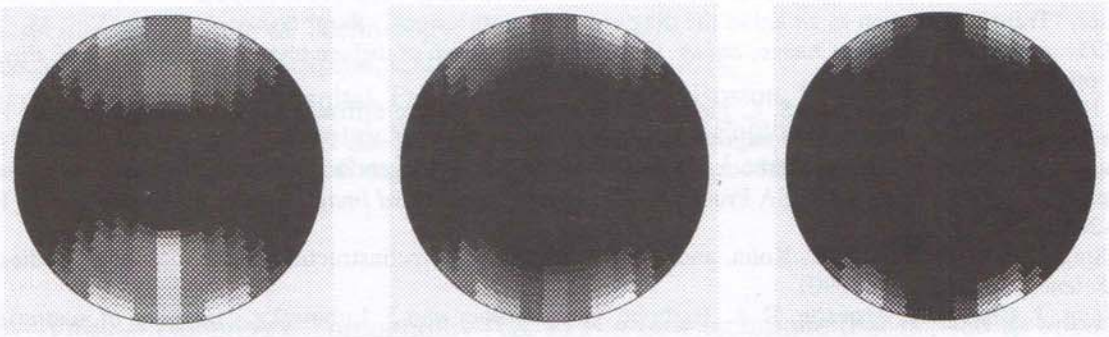

10 iterations 100 iterations 1,000 iterations

Figure 10. Gray scale display of computed cross-sectional images of the two-absorber using time-integrated data and the CGD algorithm.

For the rod-in-the-center studies, the estimated diameter of the vessel, in transport lengths, is approximately 17 and 20 for the other studies. While this error may seem small (approx. 18%), it is worth noting that the weighting functions are spatially non-linear and time-dependent. While definitive evidence is lacking, we believe that this mismatch in the assumed and "correct" weight function may have contributed for why a relatively poor image was obtained for the experiment using time-resolved measurements for the small rod phantom. The observation that the same data set, when analyzed as time-integrated data, yields a good quality image suggests that the influence of errors in the $\Delta y_i$ values and weight functions on the reconstructed image might well vary depending on the duration of the time window chosen. This suggestion is supported by the results obtained using a single time window for the off-axis rod and two rod studies. Here we observed significantly better quality images when three time windows are chosen rather than a single time window. It is worth noting that in an accompanying report [21] we describe a total least squares method that yields improved reconstructions when noise is present in both the $\Delta y_i$ values and the weight functions.

The standing question to be answered is whether clinically useful images can be obtained from thick tissue structures using optical sources. While the current studies has not answered this, we believe it is important to emphasize that the computed images were obtained using highly *underdetermined* data sets. We also note that with the exception of imposing positivity constraints, no special regularization techniques were used. These findings suggest, surprisingly, that the image recovery problem for dense scattering media may be much more stable than one might otherwise have considered.

## 5. Acknowledgment

This work was supported in part with grants to SUNY (RLB) by NIH (grant no. RO1 CA59955), the New York State Science and Technology Foundation, ONR (grant no. N0001495110063); and with grants to CCNY (RRA) by NIH, ONR, NASA/IRA and the New York State Science and Technology Foundation.

## 6. References

[1] L. Wang, P. P. Ho, C. Liu, G. Zhang, and R. R. Alfano, "Ballistic 2-D imaging through scattering walls using an ultrafast Kerr gate," *Science* **253**, 769-771 (1991)

[2] R. R. Alfano, X. Liang, L. Wang, and P. P. Ho, "Time-resolved imaging of translucent droplets in highly scattering turbid media,"*Science* , **264,** pp. 1913-1915, (1994)

[3] J. C. Hebden, "Evaluating the spatial resolution performance of a time-resolved optical imaging system," *Med. Phys* **19**, pp.1081-1087 (1992)

[4] K. M. Yoo, B. B. Das, and R. R. Alfano, "Imaging a translucent object hidden in a highly scattering medium from the early portion of the diffuse component of the transmitted ultrafast laser pulse," *Opt. Lett.* **17**, 958 (1992)

[5] B. B. Das, K. M. Yoo and R. R. Alfano, "Ultrafast Time-gated Imaging In Thick Tissues - A Step Towards Optical Mammography," *Opt. Lett.*, Vol. **18**, No. 13, p.1092-1094, 1993
[6] M. D. Duncan, R. Mahon, L. L.Tankersley, and J. Reintjes, "Time-gated imaging through scattering media using stimulated Raman amplification," Opt. Lett. **16**, 1868-1870, (1991)
[7] D. Huang, E. A. Swanson, C. P. Lin, J. S. Schuman, W. G. Stinson, W. Chang, M. R. Hee, T. Flote, K Gregory, C. A. Puliafito, J. G. Fugimoto, " Optical coherence tomography," *Science*, **254**, 1178-1181, (1991).
[8] M. Cutler, "Transillumination as an aid in the diagnosis of breast lesions," *Surg. Gynecol. Obstet*, Vol. **48**, 721, 1929
[9] M. A. O'Leary, D. A. Boas, B. Chance, and A. G. Yodh, "Refraction of diffuse photon density waves," *Physical Review Letters*, **69**, pp. 2658-2661, (1992)
[10] A. H. Hielscher, F. K. Tittel, and S. L. Jacques, "Photon density wave diffraction tomography," in OSA Proc. vol. 21, *Advances in Optical Imaging and Photon migration*, R. R. Alfano, ed. pp. 78-82, 1994.
[11] J. Chang, H. L. Graber and R. L. Barbour, "Image reconstruction of targets in random media form continuous wave laser measurements and simulated data", in OSA Proc. vol. **21**, *Advances in Optical Imaging and Photon migration*, R. R. Alfano, ed. pp. 193-201, 1994.
[12] J. R. Singer, F. A. Grunbaum, P. Kohn, and J. P. Zubelli, "Image reconstruction of the interier of bodies that diffuse radiation," *Science*, **248**, pp 990 (1990).
[13] Y. Wang, J. Chang, R. Aronson, R. L. Barbour, H. L. Graber and J. Lubowsky, "Imaging of scattering media by diffusion tomography: an iterative perturbative approach," in, *Physiological Monitoring and Early Detection Diagnostic Methods*, SPIE vol., 1641, pp. 58-71, 1992.
[14] R. L. Barbour, H. L. Graber, Y. Wang, J. Chang, R. Aronson, "A perturbation approach for optical diffusion tomography using continuous-wave and time-resolved data," Medical Optical Tomography: Functional Imaging and Monitoring, SPIE Institutes vol. IS11, pp. 87-120, 1993.
[15] R. L. Barbour, H. L. Graber, R. Aronson, J. and Lubowsky, "Imaging of Subsurface Regions of Random Media by Remote Sensing," SPIE, 1431, pp. 192-203, 1991.
[16] B. W. Pogue, M. S. Patterson, "Forward and inverse calculations for near-infrared imaging using a multigrid finite difference method," in OSA Proc. vol. 21, *Advances in Optical Imaging and Photon migration*, R. R. Alfano, ed. pp. 176-180, 1994.
[17] S. R. Arridge, "The forward and inverse problems in time-resolved infrared imaging," Medical Optical Tomography: Functional Imaging and Monitoring, ed. G. Muller, SPIE press, Bellingham, 1993
[18] J. Schotland, "Inversion formulas for diffusion imaging," accompanying paper in these proceedings.
[19] J. Chang, H. L. Graber, and R. L. Barbour, "Image reconstruction of dense scattering media from CW sources using constrained CGD and a matrix rescaling technqiue", accompanying paper in these proceedings.
[20] H. L. Graber, J. Chang, R. Aronson, R. L. Barbour, "A perturbation model for imaging in dense scattering media: derivation and evaluation of imaging operators," Medical Optical Tomography: Functional Imaging and Monitoring, SPIE Institutes vol. IS11, pp. 121-143, 1993.
[21] W. Zhu, Y. Wang, R. L. Barbour, and J. Chang, "Image reconstruction in scattering media from time-independent data: A total least squares approach", accompanying paper in these proceedings.